



Physics design of a 10 MeV, 6 kW travelling wave electron linac for industrial applications

NITA S KULKARNI*, RINKY DHINGRA and VINIT KUMAR

Accelerator and Beam Physics Laboratory, Materials and Advanced Accelerator Sciences Division,
Raja Ramanna Centre for Advanced Technology, Indore 452 013, India

*Corresponding author. E-mail: nita@rrcat.gov.in

MS received 15 July 2015; revised 5 December 2015; accepted 25 January 2016; published online 11 October 2016

Abstract. We present the physics design of a 10 MeV, 6 kW S-band (2856 MHz) electron linear accelerator (linac), which has been recently built and successfully operated at Raja Ramanna Centre for Advanced Technology, Indore. The accelerating structure is a $2\pi/3$ mode constant impedance travelling wave structure, which comprises travelling wave buncher cells, followed by regular accelerating cells. The structure is designed to accelerate 50 keV electron beam from the electron gun to 10 MeV. This paper describes the details of electromagnetic design simulations to fix the mechanical dimensions and tolerances, as well as heat loss calculations in the structure. Results of design simulations have been compared with those obtained using approximate analytical formulae. The beam dynamics simulation with space charge is performed and the required magnetic field profile for keeping the beam focussed in the linac has been evaluated and discussed. An important feature of a travelling wave linac (in contrast with standing wave linac) is that it accepts the RF power over a band of frequencies. Three-dimensional transient simulations of the accelerating structure along with the input and output couplers have been performed using the software CST-MWS to explicitly demonstrate this feature.

Keywords. Travelling wave; electromagnetic design; integrated buncher; constant impedance; longitudinal dynamics; transverse dynamics.

PACS Nos 29.20.Ej; 29.27.Bd

1. Introduction

One of the very important applications of electron linear accelerators is that they can irradiate food and agricultural products, to enhance food safety, and for better food preservation [1]. Irradiation can be done directly by the electron beam, or by X-rays generated by the electron beam. Irradiation by X-ray is preferred to the electron beam for certain applications, where greater depth of penetration is needed. Induced radioactivity in the irradiated product is not of much concern, provided the energy of the electron beam is limited to 10 MeV for the electron beam irradiation mode, and 7.5 MeV for the X-ray mode of irradiation. As the conversion efficiency from the electron beam to X-ray increases linearly with energy, it is preferred to use the electron linac with maximum permissible energy for such applications. A 10 MeV, 6 kW electron linac has been built

recently at Raja Ramanna Centre for Advanced Technology, Indore for irradiation applications. The physics design of this electron linac is described in this paper.

Radiofrequency (RF) accelerating structure is the most crucial component of an electron linac, where electromagnetic wave at RF is used to accelerate the electron beam. There are broadly two types of accelerating structures – standing wave (SW) accelerating structure and travelling wave (TW) accelerating structure [2]. In a SW linac, the RF power is fed to the structure using an RF power coupler, which sets up standing electromagnetic fields in the structure to accelerate the electrons. On the other hand, in a TW linac, RF power is fed to the structure using an input RF power coupler, which sets up a progressive electromagnetic wave in the structure to accelerate the electrons, and the power remaining at the end of the structure is dumped into a matched load, using an output RF power coupler. A simple disk-loaded waveguide is a

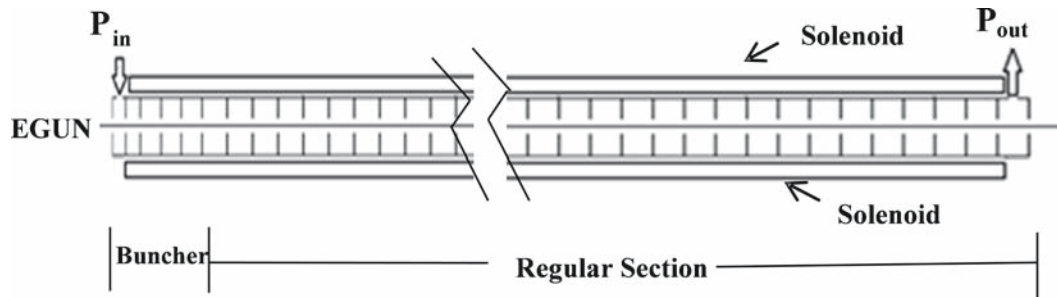


Figure 1. Schematic of the 10 MeV, 6 kW travelling wave linac.

popular choice for TW linac. Based on several considerations, such as ease of fabrication, compactness of the structure, RF power to beam energy conversion efficiency etc., SW structures are preferred for relatively low-energy applications, such as <10 MeV, and TW structures are preferred for relatively higher energy applications. A TW linac has an additional advantage that for the matched input RF power coupler, there is no reflection from the RF structure, even in transient case. This implies that no circulator is needed after the klystron in a TW linac, which results in cost reduction as circulator is an expensive microwave component. Also, the coupling of RF power to the accelerating structure in a TW linac is not affected by beam loading, unlike the SW linac. Based on these considerations, a TW structure has been chosen for the electron linac at RRCAT.

In order to make the linac compact, we have adopted an integrated buncher-cum-accelerator structure, where the low-energy beam is first bunched in the buncher cells, and then accelerated in accelerating cells. Figure 1 shows the schematic of the electron linac, and the desired parameters of the linac are shown in table 1. We have performed the electromagnetic design of the structure using electromagnetic design codes SUPERFISH [3] and CST-MWS [4]. Compared to other complicated accelerating structures, a disk-loaded waveguide-type TW linac is a relatively simple structure, which makes it possible to perform various design calculations analytically. Hence, we have performed analytical calculations for various parameters in the design, and have compared the values with the results obtained using computer codes. An extensive three-dimensional transient electromagnetic analysis of the accelerating structure along with the input and output power couplers has been done to analyse the phase advance per cell along the linac, and also to analyse the frequency bandwidth of the structure. The beam dynamics calculations have been performed using the code PARMELA [5], which are also described in this paper.

Table 1. Desired parameters of the electron linac.

Frequency (MHz)	2856.0
Structure type	$2\pi/3$ mode; Constant impedance TW
Injection energy (keV)	50.0
Output energy (MeV)	10.0
Average power (kW)	6.0
R.m.s. energy spread (%)	≤ 10
Maximum duty factor (%)	0.3

The paper is organized as follows: Section 2 discusses the electromagnetic design of the structure performed using computer codes, and also discusses some analytical calculations, which verify the results obtained using computer codes. Calculations of geometrical tolerances and heat generated on various surfaces are described in this section. Three-dimensional transient electromagnetic simulation of the accelerating structure along with the input and output RF power couplers are presented in §3. Beam dynamics studies are presented in §4. Finally, the beam parameters obtained in the linac, built on the basis of our physics design, are briefly discussed in §5, where conclusions are also presented.

2. Electromagnetic design of the accelerating structure

The linac is a $2\pi/3$ mode travelling wave structure with buncher cells followed by the accelerating cells. Operating mode is chosen as $2\pi/3$ mode because the shunt impedance of a TW linac is maximum for this case. In this mode, the phase of the travelling electromagnetic wave changes by 120° as it progresses through each cell. Design of the buncher section is important because it decides the beam characteristics at the exit of the linac [6]. An integrated TW buncher with ‘stepped phase velocity variation’ was selected.

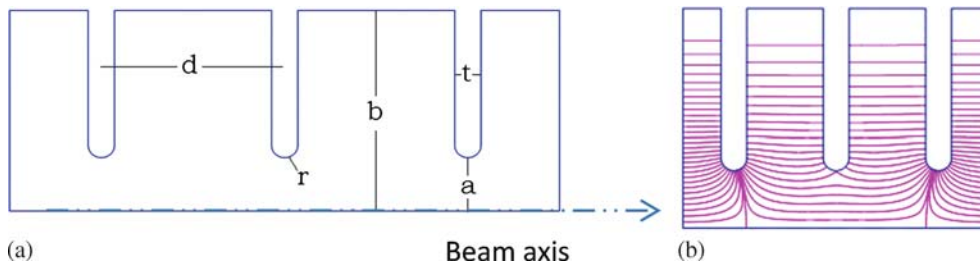


Figure 2. (a) Schematic of three cells of TW electron linac and (b) electric field configuration of $2\pi/3$ mode.

Table 2. Parameters for the linac cells.

Parameters		Buncher 1	Buncher 2	Accelerating
$2a$ (mm)		22	22	22
$2b$ (mm)		83.848	82.488	82.26
d (mm)		19.594	31.4905	34.955
t (mm)		5	5	5
r (mm)		2.5	2.5	2.5
Number of cells		2	3	45
Phase velocity/ c (β_w)		0.56	0.9	0.999
Group velocity/ c (β_g)	Analytical	0.0104	0.0109	0.0110
	Simulated	0.0108	0.0121	0.0122
Quality factor	Analytical	9467	11592	13831
	Simulated	8476	12712	13683
Attenuation (Np/m)	Analytical	0.30	0.24	0.20
	Simulated	0.33	0.19	0.18
Shunt impedance ($M\Omega/m$)	Analytical	16	41	53
	Simulated	20	52	60
Transit time factor	Analytical	0.68	0.75	0.76
	Simulated	0.75	0.73	0.72
Coupling coefficient	Analytical	0.027	0.016	0.014
	Simulated	0.023	0.015	0.014

Industrial linacs must be as compact as possible, and hence a trade-off between the length of the linac and beam characteristics was done. Schematic of the three cells ($1/2 + 1 + 1 + 1/2$) of a disk-loaded TW linac with geometrical parameters (that define the structure of the linac) is shown in figure 2a. This particular combination of three cells is used to calculate the resonant frequency and other RF parameters for the $2\pi/3$ mode. A two-dimensional electromagnetic code SUPERFISH was used to find the optimum value of these parameters. For the $2\pi/3$ mode, the cell length d is chosen as $\beta_w\lambda/3$. Here, β_w is the phase velocity of the travelling electromagnetic wave in the accelerating structure, in unit of speed of light. Resonant frequency is mainly affected by the inner diameter of the cell, $2b$, whereas the group velocity is mainly affected by the aperture diameter, $2a$. Hence, $2a$ and $2b$ are tuned iteratively to get the desired parameters. Also, $2a$ should be large enough to allow the beam to pass

through without getting intercepted. Mechanical rigidity and strength are considered while selecting disk thickness, t . The chosen geometrical parameters are given in table 2.

Beam dynamics simulations reported in §4 were performed with different configurations of buncher cells and resulted in an optimum choice of two buncher cells with $\beta_w = 0.56$, followed by three buncher cells with $\beta_w = 0.9$, as described in table 2. Using SUPERFISH, we calculated the value of $2b$ for each type of cell, such that the desired resonant frequency of 2856 MHz is achieved. Figure 2b shows the field configuration for $2\pi/3$ mode.

2.1 Calculation of RF parameters

The postprocessor in SUPERFISH is used to calculate the figures of merit of the accelerator like quality factor, shunt impedance, transit time factor etc. SUPERFISH

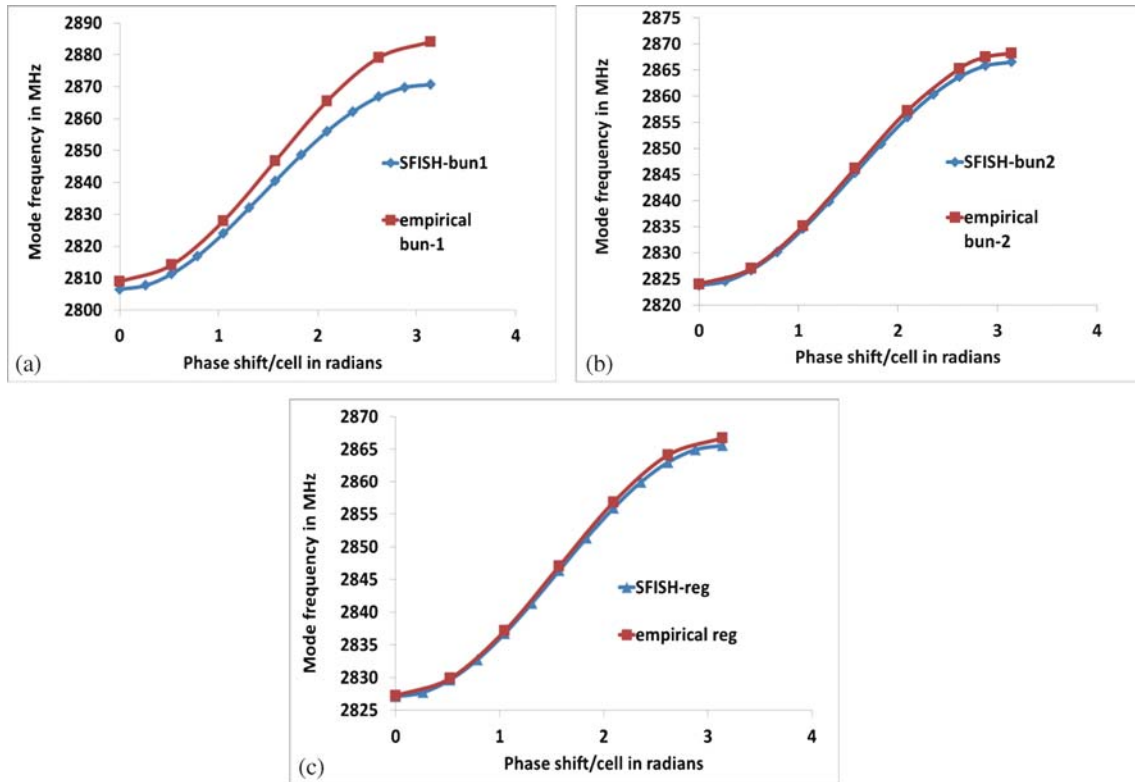


Figure 3. Dispersion diagram for a 6-cell structure, obtained using SUPERFISH, as well as empirical formula for (a) buncher type-1, (b) buncher type-2 and (c) regular cells.

performs the calculations for SW structures, and these values are then converted to the TW case. Quantities like attenuation, coupling coefficient and group velocity are derived from the simulation results, and are tabulated in table 2. These are compared with the results of analytical calculations described in the following subsection.

2.1.1 Analytical calculation of RF parameters. Expression for the resonant frequency is given by [7]

$$f_{\text{res}} = \frac{2.405c}{2\pi b} \sqrt{1 + \kappa(1 - e^{-\xi t} \cos \theta)}, \quad (1)$$

where

$$\kappa = \frac{4a^3}{3\pi J_1^2(2.405) b^2(d-t)}$$

and

$$\xi = \sqrt{\left(\frac{2.405}{a}\right)^2 - \left(\frac{\omega}{c}\right)^2}.$$

Here, θ is the phase advance per cell, J_1 is the first-order Bessel function of the first kind and c is the speed of light. Putting the design values of geometrical parameters in eq. (1), frequency of all the eigenmodes

are evaluated, and dispersion curves are plotted for the type-1 and type-2 buncher cells, and also for the accelerating cells, and are shown in figure 3. For the type-2 buncher and accelerating cells, the agreement between analytical and simulation results is excellent. The figures of merit calculated analytically differ slightly for low-phase velocities as in the case of type-1 buncher cell.

Next, we discuss the calculation of quality factor, group velocity and coupling coefficient. Expression for the quality factor is given by

$$Q = \frac{\lambda}{\delta} \frac{\beta_w [1 - (t/d)]}{n + 2.61\beta_w [1 - (t/d)]}, \quad (2)$$

where δ is the skin depth and n is the number of cells per wavelength for the desired mode. Expression for group velocity is given by

$$\frac{v_g}{c} = \frac{2(2.405)}{3\pi J_1^2(2.405)} \left(\frac{a}{b}\right)^3 \sin \theta e^{-\xi t}. \quad (3)$$

Group velocity is calculated using the above formula, as well as from the dispersion diagram drawn using simulation results. Knowing the group velocity and quality factor, attenuation coefficient A can be calculated using the expression $A = \omega/2v_g Q$. Table 2 lists the group velocity, quality factor and attenuation for

the linac cells, using analytical calculations as well as SUPERFISH simulations.

Expression for the coupling coefficient is given by

$$k = \frac{2\kappa e^{-\xi t}}{2 + \kappa}. \quad (4)$$

The coupling coefficient has been evaluated using this formula, as well as numerical simulation by using $k = (f_\pi - f_0)/f_{\pi/2}$, where f_π , f_0 and $f_{\pi/2}$ denote the resonant frequency of π , 0 and $\pi/2$ modes respectively and are obtained using simulations. For a travelling wave linac, the shunt impedance per unit length r_{sh} is given by

$$r_{sh} = \frac{Z_0^2 d}{\pi \rho_s b} \frac{T^2}{(b + d - t) J_1^2(2.405)} J_0^2\left(2\pi \frac{a}{\lambda}\right), \quad (5)$$

where the transit time factor T is given by

$$T = \frac{\sin\left(\frac{\theta}{2} \frac{d-t}{d}\right)}{\theta/2}.$$

Here, $Z_0 = 377 \Omega$ is the vacuum impedance, $\rho_s = (\pi Z_0/\sigma \lambda)^{1/2}$ is the surface resistivity, σ is the conductivity of copper and J_0 is the zeroth-order Bessel function of the first kind. In our case, $\theta = 2\pi/3$. Putting the design parameters for the buncher and regular cell in the above equations shows close agreement with the results obtained using SUPERFISH simulations, as listed in table 2. As seen in table 2, the analytical results are within 10–20% of the simulated values, and thus show good agreement, keeping in mind that the analytical formulae are approximate.

2.1.2 Calculations of power loss and geometrical tolerances. SUPERFISH is used to perform power loss calculations for standing wave structure, and these are subsequently translated to power losses on various segments in travelling wave structure. The power loss P along the cells of the buncher and regular section cells is evaluated with beam loading, as well as without beam loading. With beam loading, the peak field E at a distance z along the length of the structure is given as [8]

$$E = E_0 e^{-\tau} - I_0 r_{sh} (1 - e^{-\tau}), \quad (6)$$

where $\tau = Az$, E_0 is the electric field at the beginning of the structure and I_0 is the macropulse beam current. Note that the second term here is due to beam loading. By substituting the design values in eq. (6), the power loss along the linac can be evaluated using the relation

$$P_2 = P_1 \left(\frac{E_2}{E_1}\right)^2, \quad (7)$$

Table 3. Average power loss in the accelerating structure (duty factor is assumed to be 0.3%).

	$E_0 T$ (MV/m)	Average dP/dZ (kW/m)	
		Analytical	Simulated
Buncher type-1	7.72	11.2	13.0
Buncher type-2	9.39	6.4	6.97
Accelerating cells	9.53	5.1	6.09

where subscripts 1 and 2 represent two consecutive cells in the linac.

The average power dissipation per unit length for 0.3% duty factor is calculated using SUPERFISH simulations, and an additional safety margin of 30% was included. Power dissipated per unit length is given by the analytical formula

$$\frac{dP}{dz} = \frac{(E_0 T)^2}{r_{sh}}. \quad (8)$$

For the design values of $E_0 T$, power dissipation is calculated using the above formula. Here, the analytical values of r_{sh} given in table 2 are used. The average power dissipation is shown in table 3, and we find good agreement between the analytical and simulated values. Note that the values given in table 3 are for the first cell of the particular type. The power losses in subsequent cells are obtained using eqs (6) and (7).

Next, we discuss the calculation of tolerances on various geometrical dimensions. Random-dimensional errors produce a spread in the resonant frequency of individual cells, and this results in the reflection of the electromagnetic wave at the boundary between consecutive cells. This ultimately may result in the reduction of the amplitude of the transmitted wave, as well as a shift in phase, leading to a decrease in the energy of the accelerated beam.

Dependence of resonant frequency on cell ID ($2b$), aperture ID ($2a$) and cell length (d) is given by [6]

$$\begin{aligned} \frac{df_{res}}{d(2b)} &= -\frac{2.405c}{4\pi b^2}, & \frac{df_{res}}{d(2a)} &= \frac{2.405c\kappa}{8\pi ab}, \\ \frac{df_{res}}{d(d)} &= -\frac{2.405c\kappa}{4\pi b(d-t)}. \end{aligned} \quad (9)$$

Using eq. (9), sensitivity of the resonant frequency is estimated, which is in good agreement with the simulated values given in table 4.

Values of tolerance on various geometrical dimensions are shown in table 5. Corresponding to each of these tolerances, the frequency shift was calculated, and finally they were added in quadrature. The tolerances chosen are such that the frequency variation between

Table 4. Sensitivity of the resonant frequency with different cell dimensions.

Quantity	Simulated (MHz/mm)	Analytical (MHz/mm)
$\partial f/\partial(2a)$	8.07	8.0
$\partial f/\partial(2b)$	-36.19	-34.0
$\partial f/\partial(d)$	-2.13	-2.0

Table 5. Tolerance on various geometrical dimensions.

Disk diameter (mm)	+0.005
Bore hole diameter (mm)	± 0.005
Disk thickness (mm)	± 0.01
Cell length (mm)	± 0.01
Disk radius (mm)	± 0.005

different cells is less than 400 kHz, which is approximately the bandwidth corresponding to the quality factor of the cells.

The shift in phase resulting due to shift in resonant frequency is given by [6]

$$\Delta\theta = \frac{2\pi\lambda}{3v_g} \Delta f. \quad (10)$$

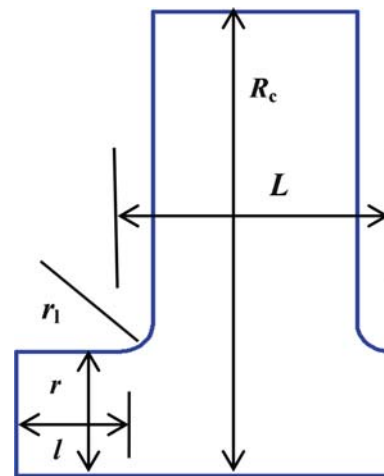
A maximum allowed frequency shift of 400 kHz resulted in a shift of about 2° for the phase advance per cell.

3. Three-dimensional simulations

In the previous section, we discussed the electromagnetic design of individual cells of the linac. As will be discussed in §4, a total number of 45 regular cells preceded by five buncher cells are required to accelerate the beam to 10 MeV with an input RF power of 4.5 MW. The crucial components of the accelerating structure are the input and output couplers. Here, the first buncher cell is used as the input coupler cell, and the last cell is used as the output coupler cell. Coupling of power is performed by having a slot in the coupler cell. Boundary conditions at the coupler cell are different from that of the adjacent cell, and therefore the inner diameter of the coupler cells is slightly modified. Detailed design of the power coupler will be reported separately [9]. Basic parameters of the input and output couplers for this linac are given in table 6 [10], and schematic of the coupler cell is shown in figures 4 and 5. Figure 5a shows the three-dimensional view of the coupler, while figure 5b shows the details of the dimensions of iris (the window that has been opened for power coupling). At the input, the RF power from

Table 6. Geometrical dimensions of the coupler cells.

Parameter	Input coupler	Output coupler
r (mm)	11	11
L (mm)	19.59	34.95
r_1 (mm)	2.5	2.5
$2R_c$ (mm)	81.27	80.75
Beam pipe length, l (mm)	7.5	7.5
Iris length, L_1 (mm)	36	36.8
Iris width, W (mm)	12	12
Iris height, H (mm)	4	4

**Figure 4.** Two-dimensional view of the coupler cell.

klystron is fed using a tapered waveguide matched to WR284 waveguide at the klystron end, and having a cross-section of 72.14 mm \times 18.00 mm at the input coupler cell [10]. At the output, the remaining RF power is fed to a matched RF load, using a tapered waveguide having a cross-section of 72.14 mm \times 22.00 mm at the output coupler cell and matched to WR284 waveguide at the matched load end [10].

Three-dimensional electromagnetic analysis of the 50-cell travelling wave structure with input and output couplers was performed using the computer code CST-MWS. Frequency domain solver with tetrahedral meshing was employed with 25 lines per wavelength resulting in the total number of tetrahedrons around 3.7 million. The S parameters namely S_{21} , where 1 and 2 refer to the input and output coupler end respectively, are plotted in figure 6, which shows a pass band, within which all the frequencies get transmitted through the travelling wave structure. This is unlike the standing wave structure, which is resonant at discrete frequencies. The 3 dB acceptance band is 2840–2864 MHz, as shown in figure 6.

The phase and magnitude of the electric field in travelling wave linac simulated using the frequency domain solver in CST MWS are used to evaluate the phase advance per cell. Electric field monitors are defined at different frequencies. Figure 7 shows the

field distribution at 2856 MHz. Figures 8 and 9 show the magnitude and phase of the electric field respectively. The phase plot is used to evaluate the phase advance per cell. The range of phase is 118° – 123° , except at the two places where it is around 114° and 116° . Barring these two points, the average phase advance per cell is 120.7° and the cell to cell variation in phase advance is around $\pm 2^{\circ}$. The variation in the phase advance is partly due to numerical error in the calculation, and partly due to a slight mismatch of the RF coupler with the accelerating structure. However, these simulations show that the accelerating structure along with the input and output couplers supports the desired electromagnetic field pattern for efficient acceleration of the beam.

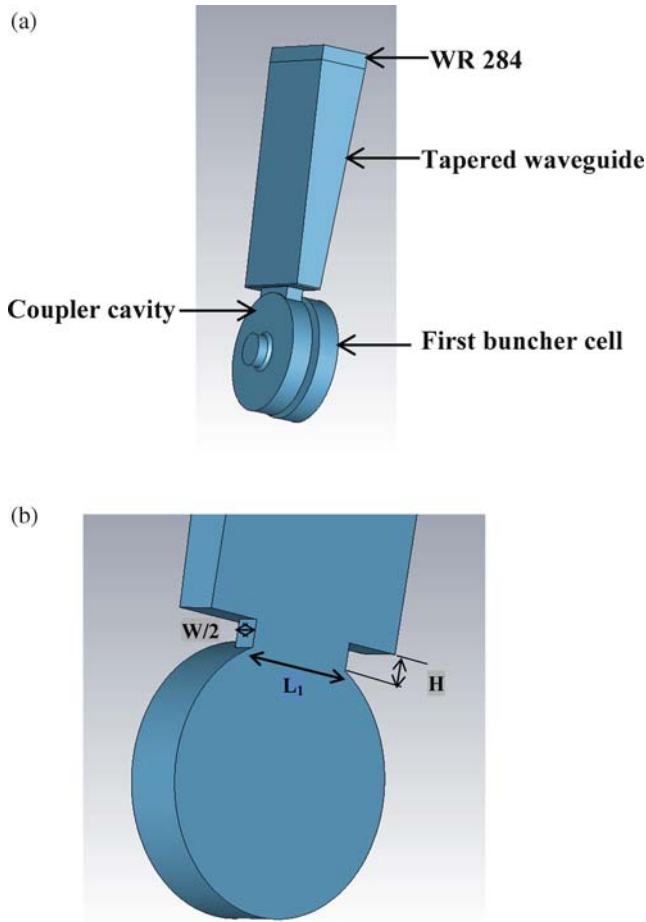


Figure 5. (a) The 3D model of the coupler with the first buncher cell and (b) magnified view of iris dimensions. W is along the direction of the beam.

4. Beam dynamics studies

The beam dynamics studies involve the study of evolution of the electron beam through the accelerating structure by tracing the motion of the particles, taking the space charge forces into account.

In designing the bunching section of the travelling wave linear accelerator, the choice of the phase velocity of RF is very important [6]. When the speed of the injected electrons is different from β_w , a particular fraction F of electrons is captured, which is termed as capture efficiency. Some of the captured electrons start moving backward towards the electron gun, and are therefore lost. The fraction of electrons that are captured, and also maintain positive velocity throughout their motion is denoted by F^+ , and is termed as the transmission efficiency. Analytical calculations have been performed to estimate the capture and transmission efficiency for different values of β_w .

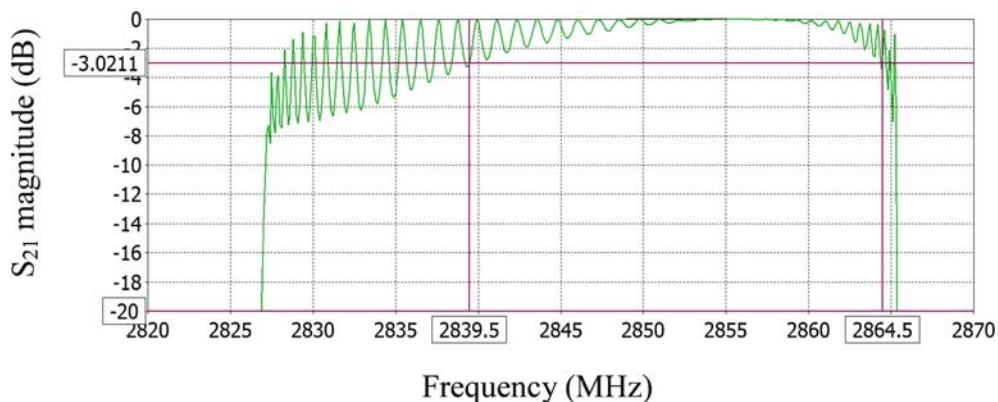


Figure 6. S_{21} characteristic of a TW linac.

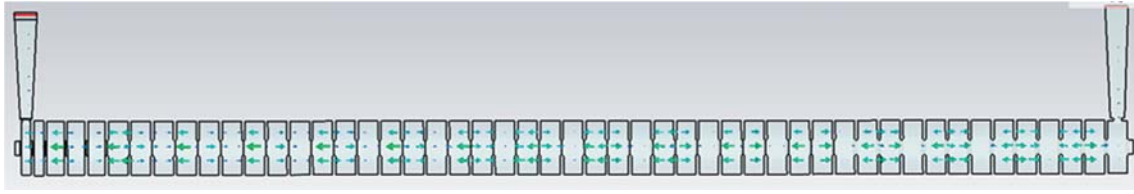


Figure 7. Electric field distribution at $f = 2856$ MHz.

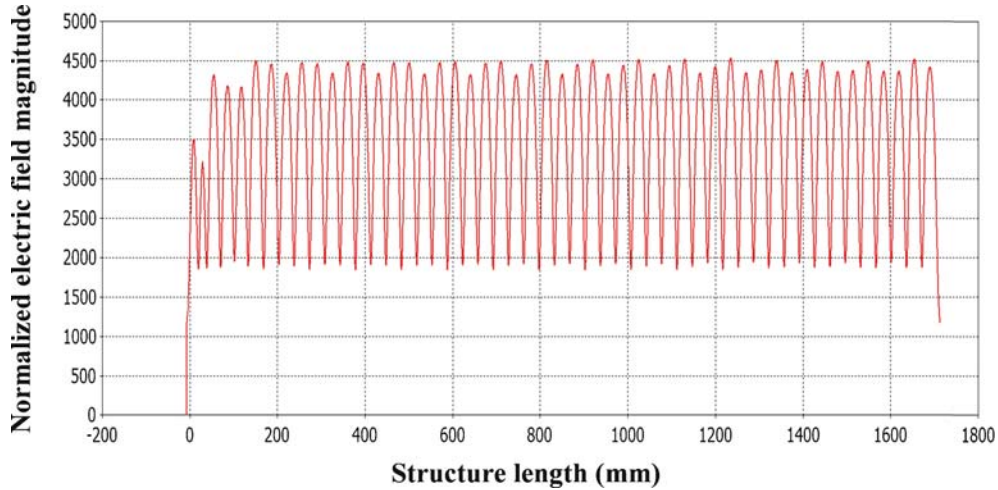


Figure 8. Normalized magnitude of longitudinal electric field amplitude along the linac length at $f = 2856$ MHz.

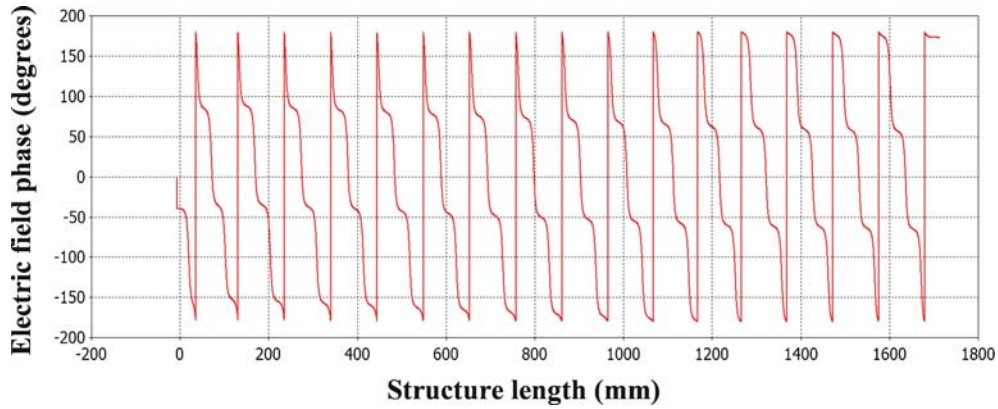


Figure 9. Phase of the longitudinal electric field along the linac length at $f = 2856$ MHz.

The fraction of captured electrons F and fraction of transmitted electrons F^+ are given by [11]

$$F = \frac{1}{\pi} \cos^{-1} \left[-1 + \frac{2\pi m_0 c^2}{\lambda \beta_w e E_z} \times \left(\sqrt{p_0^2 + 1} - \sqrt{(1 - \beta_w^2)} - \beta_w p_0 \right) \right], \quad (11a)$$

$$F^+ = \frac{1}{\pi} \cos^{-1} \left[1 + \frac{2\pi m_0 c^2}{\lambda \beta_w e E_z} \left(-1 + \sqrt{p_0^2 + 1} - \beta_w p_0 \right) \right]. \quad (11b)$$

Electrons are injected with a normalized momentum p_0 defined by $p_0 = \gamma_e m_0 v_e / m_0 c$ where v_e is the speed

of electron and γ_e is the relativistic factor corresponding to the electron beta ($\beta_e = v_e/c$). Here, m_0 is the rest mass of the electron, c is the speed of light, λ is the free space wavelength corresponding to the operating frequency, e is the electronic charge and E_z is the accelerating gradient.

The plot of F and F^+ with β_w for fixed electron velocity $\beta_e = 0.41$ and accelerating gradient $E_z = 7.97$ MV/m is shown in figure 10. The reason for this choice of E_z is described later. We notice that F becomes maximum and attains a value around 1 at $\beta_w = \beta_e$, and then reduces as β_w increases further. On the other hand, F^+ increases with β_w , and tends to

saturate. We have therefore chosen $\beta_w = 0.56$ for the first two bunchers, where F^+ is around 0.52. Figure 10 assumes that the structure is a uniform accelerating structure with a fixed phase velocity. In real case, as the beam gets accelerated, we change the value of β_w , and therefore the transmission efficiency shown in figure 10 is exceeded. We have chosen an integrated structure with stepped phase velocity in order to maximize the beam transmission. The phase velocity β_w of the next three cavities has been chosen to be 0.9 and for the rest of the structure, we have chosen $\beta_w \sim 1$. This choice is for meeting synchronization condition as electrons become relativistic quickly.

The accelerating gradient in the cavities is selected such that it is above a particular threshold E_{th} , at which the electrons start getting bound to the travelling wave, and is given by

$$E_{th} = \frac{\pi m_0 c^2}{\lambda \beta_w e} \left(\sqrt{p_0^2 + 1} - \sqrt{1 - \beta_w^2} - \beta_w p_0 \right). \tag{12}$$

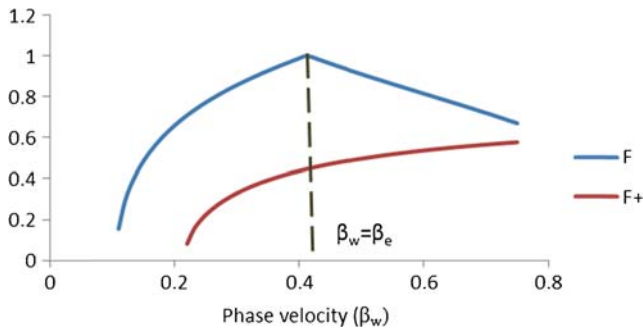


Figure 10. Variation of F and F^+ vs. phase velocity β_w for $\beta_e = 0.41$ and $E_z = 7.97$ MV/m.

The values of threshold accelerating gradient for $\beta_w = 0.56, 0.9$ and 0.999 for an injection velocity of $\beta_e = 0.41$ come out to be 0.42 MV/m, 4.3 MV/m and 9.18 MV/m respectively. The effective accelerating gradient in the cavities of phase velocity $\beta_w = 0.56, 0.9$ and 0.999 has been taken to be around 7.97 MV/m, 9.39 MV/m and 9.53 MV/m respectively, which is higher than the respective threshold values.

Next, we discuss the beam dynamics simulations of the integrated accelerating structure. Beam dynamics code PARMELA was used for these calculations, where TW fields were generated using SUPERFISH for the buncher and accelerator cells. The fringing field from the input coupler was simulated using the SW field in the first buncher cell as shown in figure 11. To get the fringe field configuration, half the buncher cell length with an additional beam pipe length is considered. Next, for generating the TW field, two eigenmodes for a one and half-cell were obtained in SUPERFISH – one with Neumann boundary condition and the other with Dirichlet boundary condition. The two fields corresponding to different boundary conditions resulted in field patterns that differ in phase by 90° . A travelling wave solution was generated by PARMELA using these two field distributions [12]. While performing the beam dynamics calculations, PARMELA scales these fields according to the value of $E_0 T$ specified in the input file. Here, $E_0 T$ is the effective accelerating field and T is the transit time factor. The field configurations for both types of boundary conditions are shown in figures 12a and 12b respectively.

Beam dynamics studies taking space charge into account were done with 5000 particles located in a phase spread $\Delta\phi$ of 360° and an energy width ΔE of

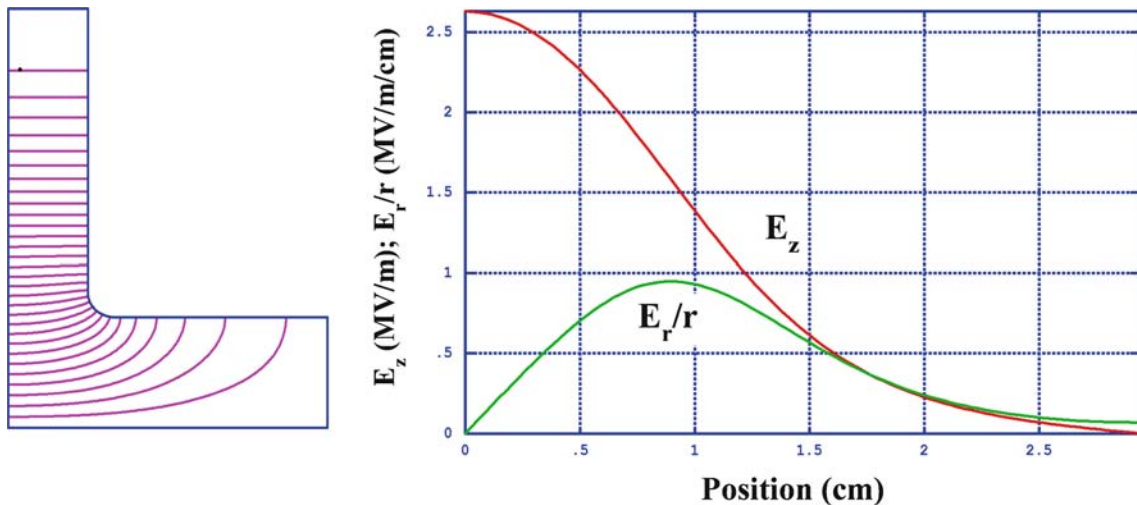


Figure 11. Standing wave field in the first buncher cell.

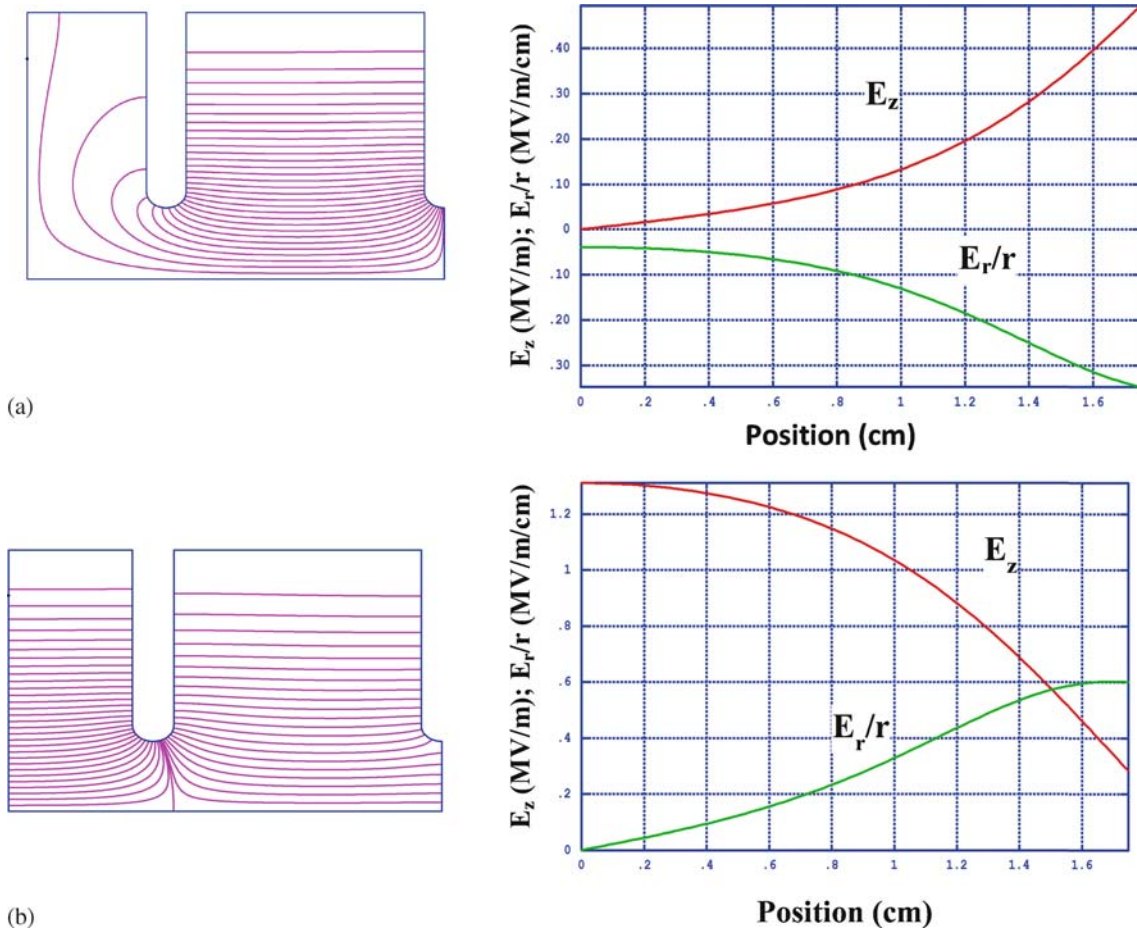


Figure 12. Field configurations obtained using (a) Dirichlet and (b) Neumann boundary conditions.

Table 7. Input beam parameters at the linac entrance.

Input energy (keV)	50
Input beam current (A)	0.32
Input r.m.s. beam size (mm)	1.58
Input r.m.s. unnormalized emittance (mrad)	3.75
Twiss parameter α	0.0
Input energy spread (%)	1.0

1%, assuming a beam waist at the entrance. A uniform particle distribution is assumed for simulating the beam and for performing beam dynamics studies.

A 50 keV DC electron gun has been developed indigenously at RRCAT. Simulation of electron gun was done using EGUN [13], and the beam parameters at the anode exit were obtained using simulations [14]. The electron beam from the exit of the electron gun is transported to the entrance of the linac structure, using a low-energy beam transport (LEBT) line, consisting of drift space and solenoid magnet, i.e. the collimator. The beam parameters at the input of the linac given

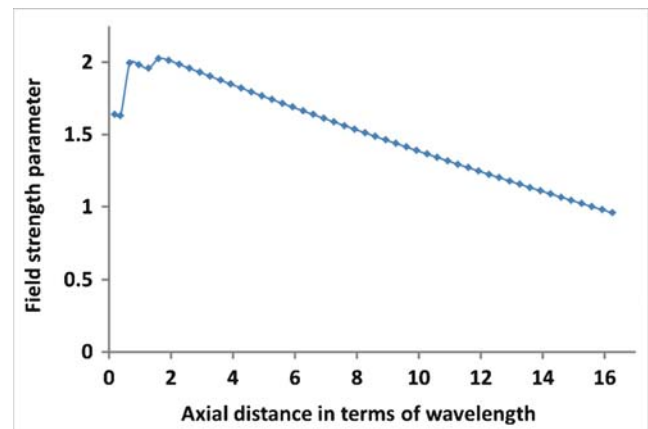


Figure 13. Field strength parameter along the length of the linac.

in table 7, were calculated using LEBT simulations [15]. The envelope equation approach was used to calculate twiss parameter α and r.m.s. beam size σ for different peak magnetic fields of the collimator. The requisite collimator field and the distance between the

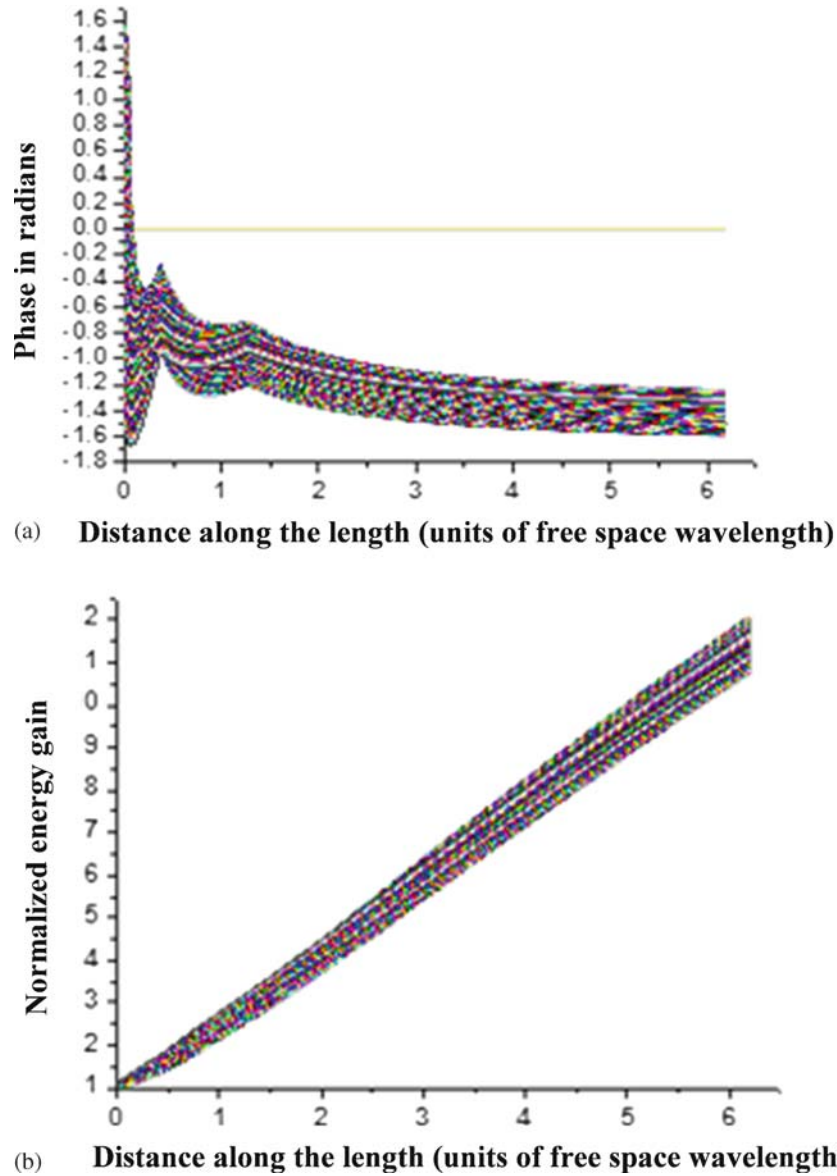


Figure 14. (a) Phase plot and (b) normalized energy gain plot, along the length of the linac.

gun and the linac entrance have been optimized in order to have a beam waist at the entry of the linac.

4.1 Longitudinal dynamics

Evolution of phase and energy of an electron is described by the following set of first-order differential equations of motion [6]:

$$\frac{d\delta}{d\xi} = 2\pi \left(\frac{1}{\beta_w} - \frac{1}{\beta_e} \right), \quad \frac{d\gamma}{d\xi} = -\alpha(\xi) \sin \delta, \quad (13)$$

where δ is the electron phase and ξ is its axial position in unit of the RF wavelength λ in free space. Here, β_w

and β_e are the phase velocity and the electron velocity respectively, in unit of speed of light, $\alpha = eE\lambda/m_0c^2$ is the field strength parameter, E is the amplitude of electric field and γ is the electron energy in unit of its rest mass energy. The function $\delta(\xi, \delta_0, \gamma_0)$ and $\gamma(\xi, \delta_0, \gamma_0)$ are determined numerically for a particular choice of field strength parameter $\alpha(\xi)$ and phase velocity $\beta_w(\xi)$ based on eq. (13). Here, δ_0 and γ_0 are initial values of δ and γ . A program was written to solve these differential equations using Runge–Kutta–Gill method, wherein space charge effect was not considered. An analytic expression for $\alpha(\xi)$, which is evaluated using the field distribution including beam loading effect

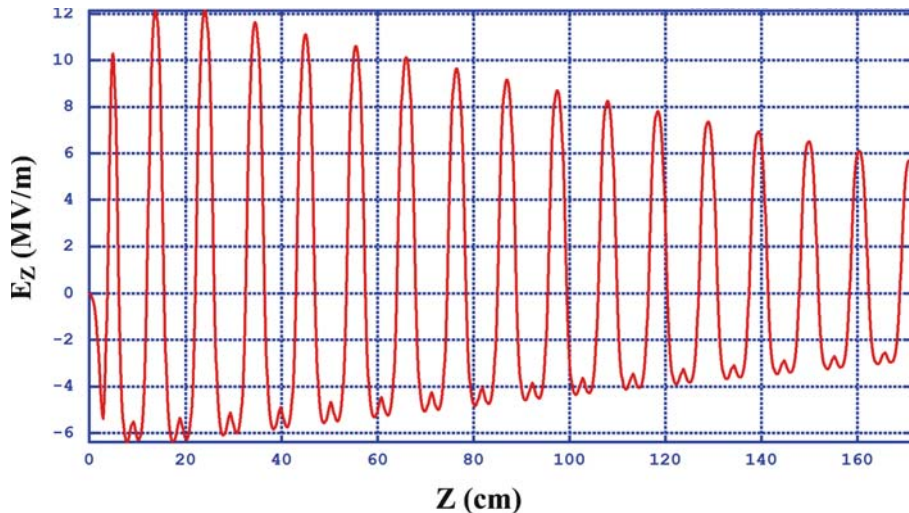


Figure 15. Electric field along the linac with beam loading.

Table 8. Output beam parameters.

Output energy (MeV)	10
Output power (kW)	6
R.m.s. beam size (mm)	1.2
R.m.s. phase spread ($^{\circ}$)	28
R.m.s. energy spread (%)	15
Transmission efficiency (%)	65

described later in this subsection, and found to have a reasonably good representation is

$$\begin{aligned} \alpha(\xi) &= -0.0848\xi + 1.6542, \quad 0 < \xi < 0.372 \\ &= -0.0836\xi + 2.0502, \quad 0.374 < \xi < 1.27 \\ &= 0.0007\xi^2 - 0.0862\xi + 2.1603, \quad \xi \geq 1.27. \end{aligned} \quad (14)$$

The field strength parameter is shown in figure 13. The phase motion of the particles with different initial phases and energy gain, calculated by solving the equations of motion, are shown in figures 14a and 14b respectively. Electrons at different injection phases travel in different orbits and finally the bunch is positioned near the peak of the RF field as seen in figure 14a.

The input power at the coupler is 4.5 MW. In a constant impedance structure, the attenuating RF power establishes a longitudinal electric field [16] given by eq. (6). The second term in eq. (6) represents the beam loading effect. The axial electric field for each of the cell is calculated by taking attenuation and beam loading into account and then used in PARMELA calculations. Figure 15 shows the electric field with beam loading. The beam loading (BL) parameter, which is

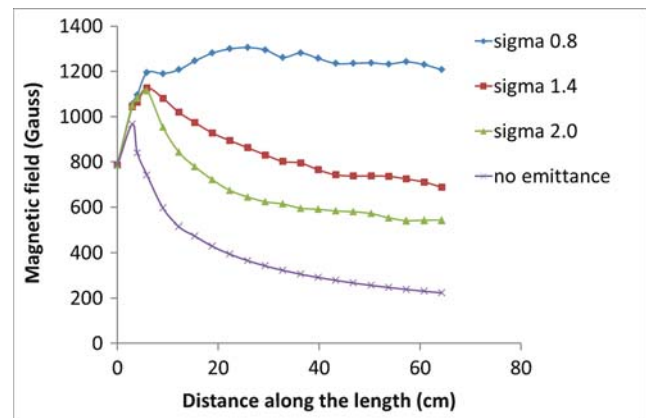


Figure 16. Magnetic field profiles obtained using the analytical formula.

the reduction in beam energy per unit increase in beam current, is given by

$$BL = r_{sh}L \left[1 - \left(\frac{1 - e^{-\tau}}{\tau} \right) \right], \quad (15)$$

where L is the length of the linac. It is seen that beam loading is dependent on length, shunt impedance and attenuation. Thus, for the given attenuation and shunt impedance of a structure, the beam loading is more for a longer structure.

With the attenuation and shunt impedance given in table 2, the beam loading parameter is found to be -14 MeV/A for an output energy of 10 MeV. With an input RF power of 4.5 MW, for a 200 mA beam current and 10 MeV output energy, a total of 45 accelerating cells were needed after the buncher cells. The total length of the linac is about 1.7 m. At the end of the linac, about 1 MW of power will be dumped in the load. The final beam parameters are listed in table 8.

4.2 Transverse dynamics

The electron beam experiences radial force due to space charge, and also due to RF fields. The radial force due to RF wave is [6]

$$F_r = eE_0 \frac{J_1(k_1 r)}{j} \frac{1 - \beta_e \beta_w}{\sqrt{1 - \beta_w^2}} \cos \Delta, \quad (16)$$

where $k_1 = (2\pi/\lambda)[(\beta_w^2 - 1)^{1/2}/\beta_w]$, $j = (-1)^{1/2}$, r is the radial position of the electron and Δ is the electron

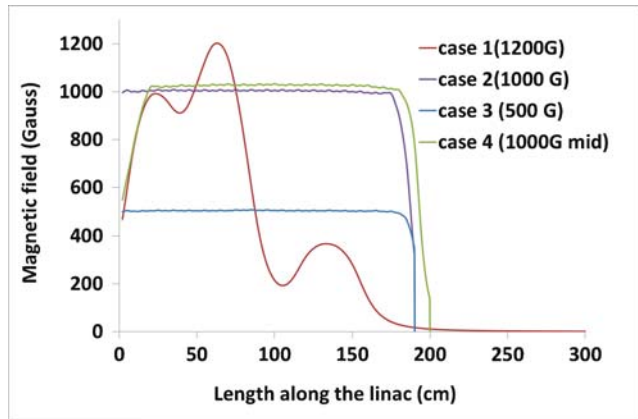


Figure 17. Magnetic field profiles assumed in the beam dynamics simulations.

phase angle with respect to the point on the travelling wave 90° ahead of the point of maximum acceleration. In the buncher, the electrons have velocities significantly less than c and thus they experience radial defocussing force and substantial beam loss will occur unless an external focussing is provided. Solenoids will be used for transverse focussing. The magnetic field profile $B(\xi)$, which keeps the beam size (σ) constant inside the linac is derived from the envelope equation, wherein the defocussing due to RF field and emittance is equated to the focussing due to magnetic field [15] and is given by

$$B(\xi) = \sqrt{2 \left(\frac{\pi E_0 T}{c\lambda(\beta(\xi)\gamma)^2} \right)^2 + \frac{\epsilon_{un,r.m.s.}(2mc\beta(\xi)\gamma)^2}{e^2\sigma^4}}, \quad (17)$$

where $\epsilon_{un,r.m.s.}$ is the unnormalized r.m.s. emittance. Variations of β , γ , $E_0 T$ and $\epsilon_{un,r.m.s.}$ inside the TW linac have been obtained from the beam dynamics calculations performed using the computer code PARMELA. These values are substituted in eq. (17) to calculate the required magnetic field profile along the length of the linac. Note that our formula for the magnetic field profile is more general compared to the

Table 9. Output beam parameters for different field profiles.

Beam parameters	$B_{z,max} = 1200$ G	$B_{z,max} = 1000$ G (mid-position)	$B_{z,max} = 1000$ G	$B_{z,max} = 500$ G
R.m.s. beam radius (mm)	2.0	1.2	1.73	1.7
Maximum r.m.s. beam radius (mm)	2.02	1.9	1.95	2.6
Unnormalized r.m.s. beam emittance (cm rad)	0.00032	0.000337	0.000488	0.000336
R.m.s. energy spread (%)	15	16	16	15
R.m.s. phase spread (°)	27	28	28	28
Transmission efficiency (%)	64	65	65	64

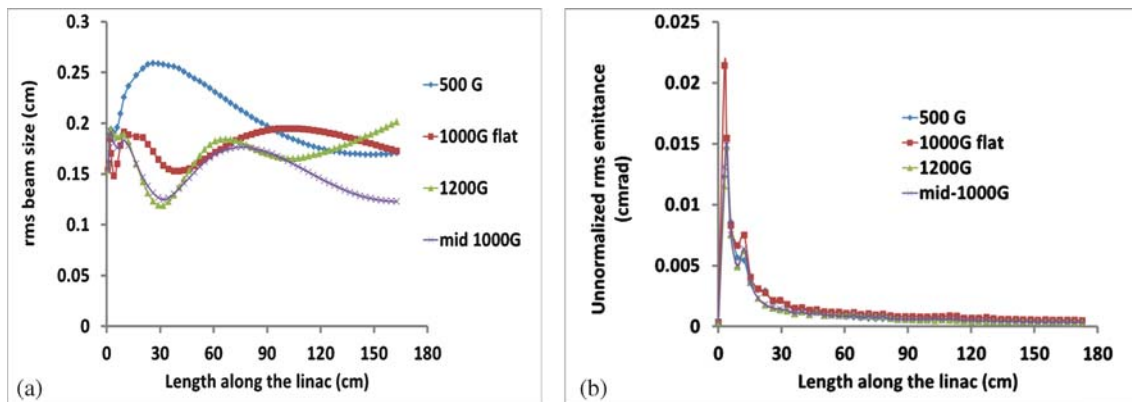


Figure 18. (a) R.m.s. beam size and (b) unnormalized r.m.s. emittance along the length for different magnetic field profiles.

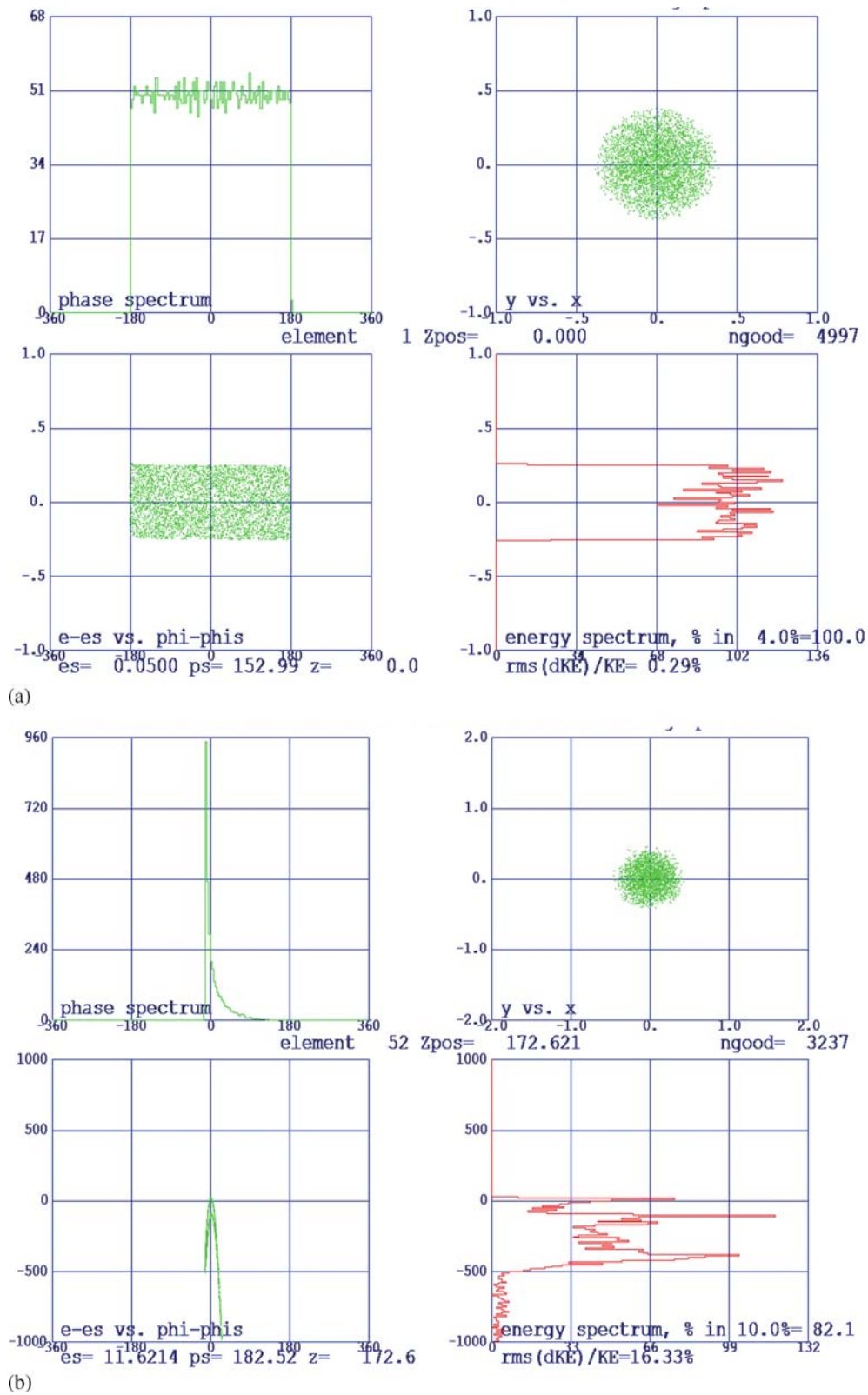


Figure 19. Transverse phase-space and phase and energy spectrum plots for (a) the first cell and (b) the last cell of the linac.

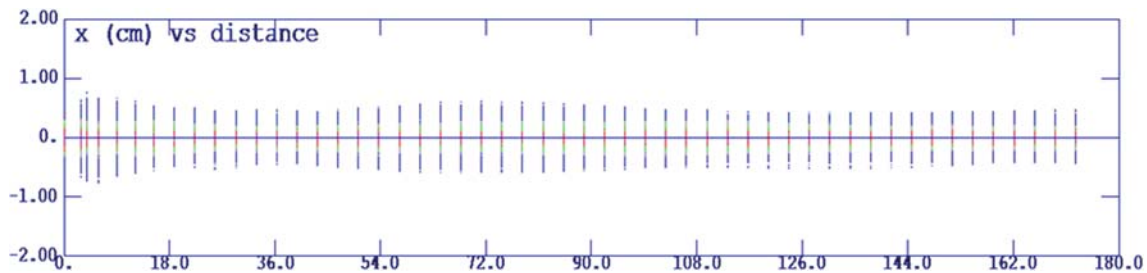


Figure 20. Evolution of horizontal beam size along the length of the linac.

widely used formula given in ref. [6], where the emittance term is absent. Figure 16 shows the analytically calculated magnetic field profiles for r.m.s. beam size of 0.8 mm, 1.4 mm and 2.0 mm. Based on the results presented here, a variable magnetic field profile with a peak value of around 1200 G is recommended.

Simulations were performed with different profiles of the magnetic field to limit the beam size, thus minimizing the loss. Figure 17 shows the simulated magnetic field profiles along the length of the linac for different magnetic fields. Table 9 shows the output beam parameters for these magnetic field profiles. The transmission efficiency in the absence of magnetic field is 43%, which increases to about 65% in the presence of external solenoidal field. Figure 18a shows the r.m.s. beam radius and figure 18b shows the unnormalized r.m.s. emittance, along the length for different magnetic field profiles. Figure 19 gives the transverse phase-space plots and the phase and energy spectrum at the input and output of the linac. Figure 20 shows the evolution of horizontal beam size along the length of the linac.

It is seen that the phase and energy spread is large due to increased phase oscillations. The phase spread can be minimized using a pre-buncher followed by a travelling wave buncher. A re-entrant kind of pre-buncher cavity followed by a drift distance can be used after the electron gun for bunching the electron beam to improve the capture. Pre-buncher typically enhances the transmission efficiency up to 80–90%. This will however need two RF feedpoints in the accelerator.

5. Results and conclusion

The accelerating structure has been built according to the design described in this paper, and is currently undergoing commissioning. The beam energy was measured as 9.0 MeV and beam current at the linac exit was measured as 200 mA [17]. The beam transmission efficiency was measured to be around 60%.

During the commissioning phase, the linac has been operated at 150–200 Hz, instead of the design value of 300 Hz. In order to get high average power even at lower repetition rate, the linac was operated at 300 mA. For this case, the beam energy was 8.0 MeV. Reduction in beam energy at higher beam current is expected to be due to beam loading. The average electron beam power of ~4 kW has been achieved at the exit of the linac.

To summarize, in this paper, we have presented the design of a 10 MeV, 6 kW travelling wave electron linac. Details of the design calculations using computer codes as well as analytical techniques have been discussed. Some of the important aspects of a travelling wave linac have been highlighted with the help of elaborate calculations. Results obtained during the commissioning trial of the accelerating structure validate its design. In future, we propose to work on the design of a pre-buncher to improve the beam transmission efficiency and beam energy spread.

Acknowledgements

It is a pleasure to thank Dr S B Roy for critical reading of the manuscript and useful suggestions. The authors sincerely thank Dr P D Gupta, Director, RRCAT for constant encouragement and support. They also sincerely acknowledge various useful discussions with P K Jana, C B Patidar and Y C Nie and also acknowledge the colleagues from Industrial Accelerator Section, Pulse High Power Microwave Division and various other expert groups of RRCAT for their effort in the facility development.

References

- [1] R B Miller, *Electronic Irradiation of foods – An Introduction to the technology* (Springer, 2005)
- [2] Roger H Miller, *Comparison of standing wave and travelling wave structures*, SLAC-PUB-3935 (1986)
- [3] J H Billen and L M Young, POISSON/SUPERFISH, LA-UR-96-1834, Revised January 13, 2006

- [4] CST Studio Suite 2008, Publisher: CST GmbH, Version 1.2.2
- [5] Lloyd M Young, PARMELA-LA-UR-96-1835, LANL
- [6] M Chodorow *et al*, *MARK-III*, RSI-Vol. 26, No. 2, 1955
- [7] Thomas Wangler, *RF linear accelerators* (Wiley, 2008)
- [8] Perry B Wilson, SLAC-PUB-2884, February 1982
- [9] P K Jana *et al*, *Design of RF power couplers for a 10 MeV, 6 kW travelling wave electron linac* (to be published)
- [10] P K Jana *et al*, *Design of RF power coupler for 5 MeV, 3 kW travelling wave electron linac*, Indian Particle Accelerator Conference INPAC, 2013
- [11] Georges Dome, *Electron bunching by uniform structures of disk loaded waveguide*, Technical Report No. M-242-A, Stanford University
- [12] G A Loew *et al*, *IEEE Trans. Nucl. Sci.* **NS-26(3)**, 3701 (1979)
- [13] W B Herrmannsfeldt, EGUN: An Electron optics and Gun design program-SLAC-331
- [14] Y Wanmode and T S Reddy, Private communication
- [15] Chirag Bhai Patidar, Nita S Kulkarni and Vinit Kumar, *Beam transport calculations for the low energy beam transport line for a 10 MeV linac*, Internal Report No. RRCAT/2015-01
- [16] G A Loew *et al*, *Elementary principles of linear accelerators*, SLAC-PUB-3221
- [17] Jishnu Dwivedi, Status of electron beam irradiation facility under development at RRCAT, NAARRI – International Conference on State-of-the-Art Radiation Processing, NIC-STAR 2015, 4–6 March 2015 (Mumbai, India)